Bulletin of Geophysics and Oceanography Vol. XX, n. X, pp. XXX-XXX; Xxxxx 20xx
DOI 10.4430/bgo00519

Estimation of the 2016 Paraná River (Argentina, South America) flood extent using satellite imagery, band fusion, and spectral indices

S. Mendizabal

Department of Risk Management, Municipality of Santa Fe, Santa Fe de la Vera Cruz, Argentina

(Received: 11 March 2025; accepted: 27 November 2025; published online: 15 April 2026)

ABSTRACT In January 2016, the Paraná River caused flooding in the city of Santa Fe, Argentina, affecting areas bordered by the Colastiné River and Setúbal Lagoon, both located within the alluvial valley of the Paraná. The gauges registered the peak flood during this event; however, a precise spatial delineation of the flood extent was not captured. Therefore, this study aimed to estimate the flood extent and identify the affected areas. In this manner, Sentinel-2 imagery was used, and a high-pass filter was applied to enhance the resolution of the short-wave infrared bands from 20 m to 10 m. The fusion was evaluated using the quality-without-reference index, yielding an accuracy above 81%. Several spectral indices, including the automated water extraction index (AWEI), desert flood index, modified normalised difference water index, new water index, normalised difference water index, and water ratio index, were compared. AWEI demonstrated the highest overall accuracy (97.4%) and Kappa coefficient (94.9%), indicating excellent agreement with ground-truth data. Subsequently, the floodline was overlaid on a 5 m resolution digital elevation model to extract the lowest elevations within the affected areas, which were hypothesised as the initial water ingress locations. The flood impacted areas in the La Costa district and the NW of Setúbal Lagoon, all situated outside the levee system. The results of this study could enable local authorities to anticipate the impacts of future flood events.

Key words: flood mapping, high-pass filter, QNR-index, R programming language, Sentinel-2 imagery, spectral indices.

1. Introduction

The El Niño-Southern Oscillation (ENSO) phenomenon is the dominant mode of interannual climate fluctuation worldwide, driven by a complex ocean–atmosphere interaction and exerting significant global influence (Gergis *et al.*, 2006; Pántano *et al.*, 2022; Hurtado *et al.*, 2023; Montanher *et al.*, 2023) as it oscillates between the El Niño (EN) and La Niña (LN) phases. EN tends to be associated with above-average precipitation, while LN is typically linked to below-average precipitation. During the EN phase, the eastern equatorial Pacific region typically exhibits an increase in precipitation (Santoso *et al.*, 2017), with intensified variability during the boreal winter (December–February) (D'Arrigo *et al.*, 2005). The variability observed during the 20th century appears to exhibit greater intensity than that recorded in earlier periods. A notable climatic shift occurred during the 1970s and persisted until the late 1990s, marked by a transition to a more positive phase of the Pacific Decadal Oscillation, which significantly influenced the

properties and dynamics of the ENSO (Santoso *et al.*, 2017). Starting in that decade, there is evidence of an increase in the frequency and intensity of ENSO-related events (Gergis *et al.*, 2006; Santoso *et al.*, 2017; Isla, 2018; Lovino *et al.*, 2022), which translated into an average increase in precipitation, particularly after the extreme event of 1982–1983. Subsequently, precipitation levels stabilised, notably over Argentina (Boulanger *et al.*, 2005). This trend highlights a marked uneven distribution of mean annual precipitation across the Paraná Basin, with maximum values occurring in the eastern sector (Pasquini and Depetris, 2010).

The year following a strong EN event is generally characterised by an increase in the discharge of rivers, often exceeding average volumes, as observed in the Paraná River (Amarasekera *et al.*, 1997). Accumulated rainfall in the upper Paraná Basin (upstream of the city of Corrientes, Argentina) leads to extreme discharges (Depetris *et al.*, 1996; Prieto, 2007), which in some cases can exceed more than double or even triple the monthly average volume (Camilloni and Barros, 2003). This intensification of extreme discharges contributes to profound hydrological changes in the Paraná River, including more frequent flood events and altered discharge patterns, primarily attributed to climate change, which leads to an increased regional rainfall (Anderson *et al.*, 1993; Tucci and Clarke, 1998; Depetris, 2007; Abou Rafee *et al.*, 2022). Notably, the Paraná River experienced multiple severe flooding events, particularly in 1983, 1998, and 2016, each preceded by intense EN events in 1982, 1997, and 2015, respectively.

The 2015–2016 El Niño (EN15-16) was the most intense of the 21st century, offering the scientific community an opportunity to reassess the understanding of the event by comparing it with previous events (Martínez *et al.*, 2017). As a result, catastrophic consequences were observed in the middle and lower sections of the Paraná River (downstream of Corrientes), significantly impacting the riverside cities, with Santa Fe de la Vera Cruz (hereinafter referred to as Santa Fe) being the most affected (Province of Santa Fe, 2016). In February and March 2015, local precipitation inundated several areas in Santa Fe, which were mapped with high precision through field surveys. By late 2015, the Paraná began to rise, reaching its peak level in January 2016, which induced the overflow of dependent hydrological systems and inundation of riverine neighbourhoods (Neffen, 2016). The mapping of these flood-affected areas is less precise than that of the 2015 precipitation events, as the 2016 floods primarily impacted sparsely populated riparian zones, whereas the 2015 precipitation events affected densely populated residential neighbourhoods. Consequently, there is limited information on the spatial extent of the 2016 flood in the city of Santa Fe.

The lack of historical data, both for this event and for previous occurrences, hinders local authorities from establishing a reliable baseline to support the development of strategic preventive measures for future flood events. This is concerning for two reasons. First, between 2019 and 2023, the north-eastern region of Argentina experienced a LN event, characterised by prolonged drought conditions and a substantial recession of local hydrological systems. This phenomenon exposed extensive land areas, facilitating the unauthorised sale of parcels in these non-developable, flood-prone zones along the Colastiné River (Aire Digital, 2020). As a consequence, the population is expanding near the minor bed of watercourses, increasing its exposure to flood hazards. Moreover, in 2023–2024, an event of the EN occurred, thus significantly increasing the risk of flooding. Given the circumstances, it is crucial to accurately identify potentially flood-prone areas to improve the existing evacuation plans, develop community awareness, and ensure effective coordination with emergency services. Second, current climate change projections suggest an escalation in the frequency and intensity of ENSO events. According to the Sixth Assessment Report of the Intergovernmental Panel on Climate Change, heavy precipitation events, river floods, and coastal floods are projected to intensify in

the south-eastern region of South America with medium confidence (Table TS.5 of Arias *et al.*, 2021). The strong correlation between extreme precipitation and flood occurrences indicates a concurrent escalation in both their frequency and intensity. Consequently, assessing spatial patterns and delineating flood-prone areas becomes increasingly crucial. Moreover, this trend highlights the urgent necessity to strengthen response capacities to future extreme flooding events, which may be comparable to, or even exceed, the severity of the 2016 flood. Therefore, the core research question of the present study is: how can the spatial delineation of the 2016 flood event in the city of Santa Fe be accurately reconstructed to identify the flooded areas and the currently urbanised areas potentially at risk of future flooding?

Several studies concentrated on the social dimensions of the flood risk in the city of Santa Fe (Baez Ullberg, 2017; Crovella and Acebal, 2018*;* Filippi, 2022; Gardiol and del Valle Morresi, 2023), highlighting the adverse social impacts of recurrent flooding. Nevertheless, scientific research addressing how these social impacts could be mitigated through informed decision-making remains limited. Moreover, the city exhibits a scientific gap regarding the spatial extent of flood events that impacted it. Graosque and Guasselli (2020) mapped the 2016 flood event in Santa Fe, achieving a classification accuracy of 70%. However, this degree of accuracy is insufficient for the precise delineation of the complete spatial extent of the flood event. Additionally, their analysis was based on images that were not captured when water levels peaked and the authors acknowledged that their methodological approach had limitations when applied to urban environments. Similarly, Fonnegra Mora *et al.* (2021) explored the spatiotemporal monitoring capabilities of spectral indices in relation to hydrological risk in Santa Fe during the 2016–2021 period. While their study provided valuable insights, it did not specifically assess the extent of water coverage on the date closest to the peak flood event in 2016. Thus, to date, no study with precise results on the 2016 flood has been conducted in Santa Fe.

Remote sensing is one of the most widely adopted techniques for estimating the spatial extent of flood events. Consequently, it is chosen as the primary approach to respond to the core question of this study, as it enables the extraction of pixels corresponding to water bodies at a given moment. To this end, various techniques are extensively used in urban environments. Several studies explored different remote sensing and spatial analysis techniques to assess flood risk and water body detection. Some studies performed multi-temporal analyses to monitor water body dynamics and flood evolution (Ferral *et al.*, 2019; Auwalu *et al.*, 2021; Kabeja *et al.*, 2022; Subraelu *et al.*, 2023), while others employed synthetic aperture radar imagery to delineate flood extents in urban areas (Mason *et al.*, 2021; Zhao *et al.*, 2022). The use of Sentinel-1 data also proved effective for flood mapping and water detection (Zhang *et al.*, 2021). In addition, several authors applied supervised and unsupervised classification methods (Sukojo and Alfiansyah, 2017; Tanim *et al.*, 2022) and spectral water indices (Jain *et al.*, 2005; Ji *et al.*, 2009; Alganci *et al.*, 2019; Khalid *et al.*, 2021; Erkoç, 2023) to improve accuracy of water body extraction.

In this context, the present research focuses on evaluating the effectiveness of various water spectral indices in estimating the spatial extent of the 2016 Paraná flood. Building upon this methodology, the study aims to generate a high-resolution map delineating flood-affected zones, thereby facilitating the advancement of early warning systems and enhancing spatial planning within the city of Santa Fe. Simultaneously, it establishes a comparative framework that could be potentially useful for globally evaluating other urban areas that experience analogous flooding events. As a result, the findings of this research will increase the understanding of urban environmental responses to extreme hydrological events.

2. Study area

The Paraná Basin is the second largest basin in South America, after the Amazon Basin, encompassing an area of 2.63 million km^2. The Paraná River originates in the high plateaus of the state of Minas Gerais, Brazil, and flows southwards, forming the border between Brazil, Paraguay, and Argentina (Fig. 1). It converges with the Paraguay River near the city of Corrientes, Argentina, before continuing towards the delta of the La Plata River, and reaching the Atlantic Ocean. According to the Sistema Nacional de Información Hídrica (SNIH, 2025), the long-term average discharge of the Paraná at the Corrientes section for the period 2000–2024 is 17,458 m^3/s.

The city of Santa Fe is located within the Paraná floodplain, 600 km downstream from Corrientes. From west to east, its boundaries are defined by the Salado River, the Setúbal Lagoon, and the Colastiné River, the latter being a branch of the Paraná. The city is characterised by low-lying terrain, with elevations ranging approximately between 12 and 24 m m.s.l. (mean sea level). According to the most recent census conducted by the Instituto Nacional de Estadística y Censos de la República Argentina (INDEC, 2023) in 2022, the population of Santa Fe exceeded 400,000 inhabitants. The geographical setting, combined with decades of inadequate or absent urban planning, renders Santa Fe highly vulnerable to hydrometeorological hazards (De Majo, 2022).

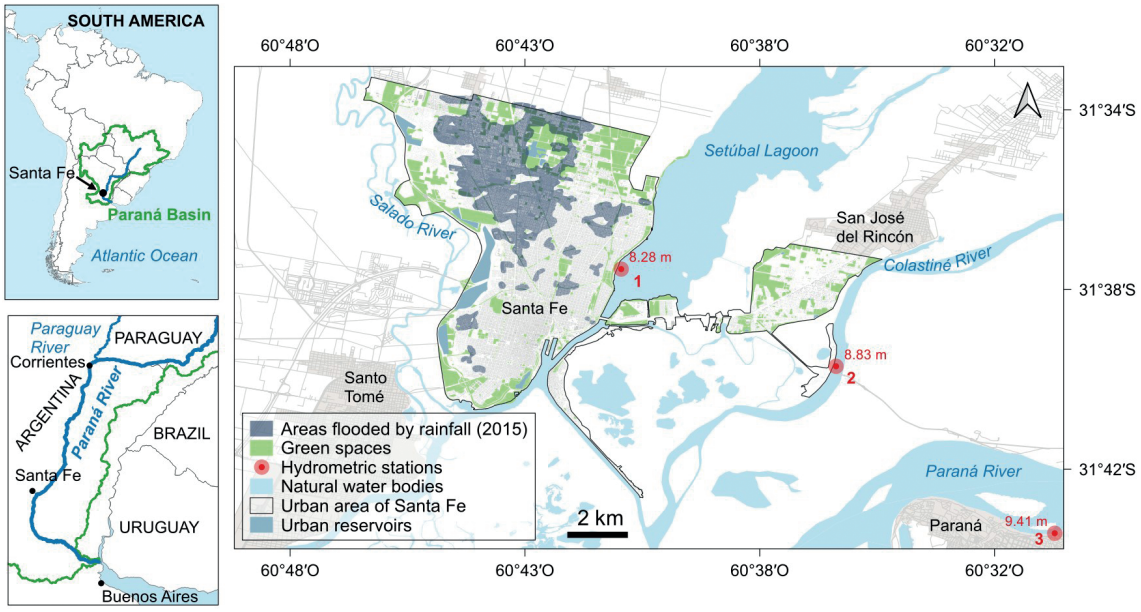

Fig. 1 - Location map of the Paraná Basin (green outline) and the city of Santa Fe (black outline), showing the three gauges with their respective reference vertical datum levels [red points, in metres mean sea level (m.s.l.)], and the flooded areas resulting from intense rainfall events during February and March 2015 (dark blue area).

In early 2015, Santa Fe experienced intense local rainfall, reaching a peak intensity of 177 mm/h on 25 February, according to internal reports from the Department of Risk Management of the Municipality of Santa Fe. This rainfall event, combined with a deficient drainage system obstructed by garbage, led to the flooding of several residential neighbourhoods (dark blue

area in Fig. 1). This was one of many risk scenes that prompted the Municipality of Santa Fe to adhere to the Sendai Framework for Disaster Risk Reduction 2015-2030, which establishes a comprehensive approach to reduce disaster risk through a series of specific actions (UNDRR, 2015). By late 2015, the discharge of the Paraná River began to increase, eventually reaching a peak discharge of 25,478 m^3/s on 1 January 2016, at hydrometric station no. 3 (Fig. 2). Furthermore, on 25 December 2015, the Setúbal Lagoon surpassed the established alert threshold of 5.3 m, and, by 28 December, it reached the evacuation threshold of 5.7 m. The water level continued to rise, peaking at 6.85 m on 5 January 2016, a level that was maintained until 8 January (SNIH, 2025). Simultaneously, the Colastiné River exceeded the alert threshold on 24 December 2015, surpassed the evacuation threshold on 28 December, and continued to rise, reaching a maximum level of 6.66 m on 8 January 2016 (SNIH, 2025). This led to the flooding of inhabited riverine areas classified as flood-prone according to Ordinance No. 12591 (Honorable Municipal Council of the City of Santa Fe de la Vera Cruz, 2018), as well as public green spaces, open riparian areas, and riverfronts. During this period, the Salado River did not reach maximum levels or cause flooding, therefore it was excluded from the analysis.

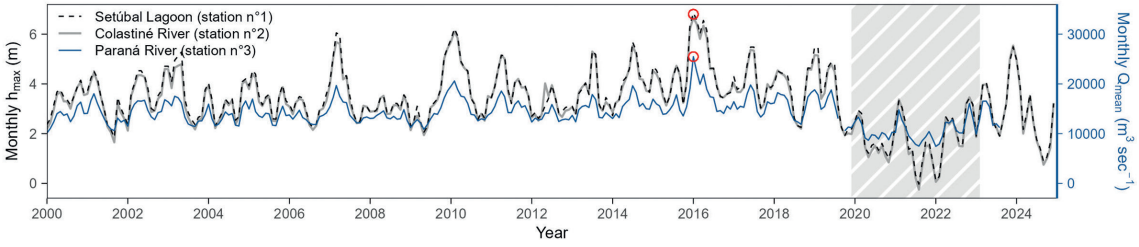

Fig. 2 - Time series (2000–2024) of the maximum monthly water levels of the Colastiné River (grey curve) and Setúbal Lagoon (black dashed curve), along with the mean monthly discharges of the Paraná River (blue curve). These series detected the extraordinary flood event of 2016 (red circles) and the La Niña phase (grey shaded area).

Finally, between late 2019 and early 2023, the city experienced a LN phase, resulting in a substantial decrease in water levels (grey shaded area in Fig. 2). This decline exposed extensive land areas, where the population expanded along the minor bed of watercourses, thereby increasing its exposure to flood hazards.

3. Data and methodology

The data processing and analysis procedures are executed using an automated approach with the R programming language, version 4.2.2. This method is implemented to streamline the process and mitigate errors throughout all phases of the process. The main libraries include: dplyr (Wickham *et al.*, 2023), ggplot2 (Wickham, 2016), purrr (Wickham and Henry, 2023), raster (Hijmans, 2023), and sf (Pebesma, 2018).

Fig. 3 shows the flowchart of the approach in detail.

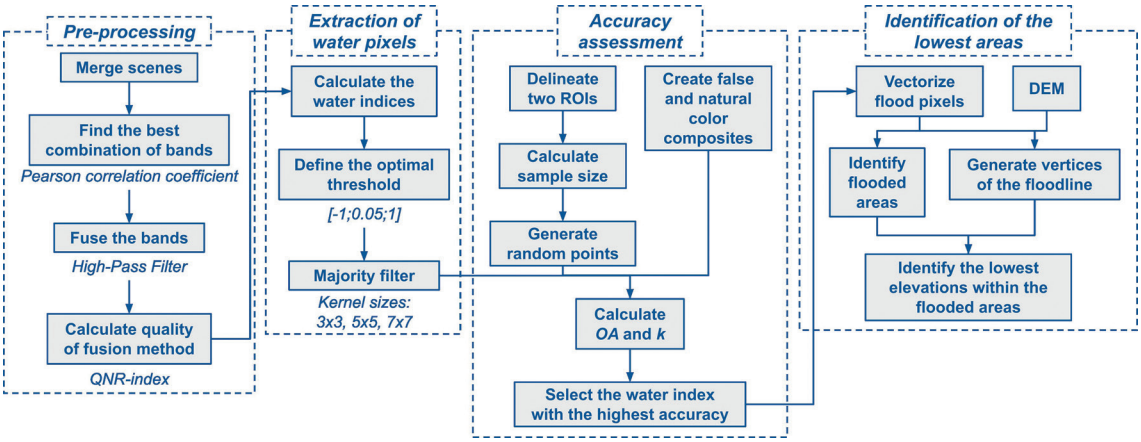

Fig. 3 - Flowchart of the approach.

3.1. Preprocessing of the satellite imagery

Two Sentinel-2 multi-spectral instrument level-2A scenes from 13 January 2016, capturing data across 13 spectral bands, including the visible near-infrared (VNIR) and short-wave infrared (SWIR), are retrieved from the Copernicus Data Space Ecosystem browser (CDSE, n.d.). This date is the closest to the peak flood recorded on 8 January, with no cloud cover in the study area. Table 1 illustrates the maximum water levels recorded on 8 and 13 January, along with the vertical datum of gauge, so these two scenes are mosaicked to cover the study area.

Table 1 - Comparison of maximum water levels recorded by gauges on 8 and 13 January 2016.

Hydrological systems	Vertical datum of the gauge (m m.s.l.)	Maximum water levels recorded on 8 January (m)	Maximum water levels recorded on 13 January (m)
Colastiné River	8.83	6.66	6.51
Setúbal Lagoon	8.28	6.85	6.75

VNIR bands have a resolution of 10 m, while the SWIR bands with central wavelengths of 1.610 µm (SWIR1) and 2.190 µm (SWIR2) have a resolution of 20 m. To enhance the resolution of the SWIR bands to 10 m, a band fusion is applied. This process involves integrating the spatial characteristics from a higher-resolution band (hereinafter referred to as the panchromatic band or *PAN*-like band, as it is not necessarily a true panchromatic band) with the spectral characteristics from a lower-resolution band, in this case, the SWIR bands [hereinafter referred to as multispectral (*MS*) bands]. As no high-resolution *PAN*-like band is available for the study area, an alternative approach is adopted, utilising one of the VNIR bands as a *PAN*-like band. This procedure has already been adopted, for example, by Yang *et al.* (2017), who used the green band as a *PAN*-like band for the fusion of the SWIR1 band and the near-infrared (NIR) band for the fusion of the SWIR2 band, based on their strong spectral correlations. Furthermore, Du *et al.* (2016) applied a similar technique, using the NIR band for the fusion of the SWIR1 band.

These literature-based band combinations are evaluated, and the Pearson correlation coefficient (*r*) is calculated to determine the strength of the relationships between the bands and identify the combination yielding the best correlation (Table 2):

$$r = \frac{\sum_{i=1}^{N}(x_i-\bar{x})(y_i-\bar{y})}{\sqrt{\sum_{i=1}^{N}(x_i-\bar{x})^2 \sum_{i=1}^{N}(y_i-\bar{y})^2}} \quad (1)$$

where *r* varies between -1 (negative correlation) and 1 (positive correlation), x_i is the original *MS* band, $\bar{x}$ is the mean value of the original *MS* band, y_i is the upscaled *PAN*-like band, resampled to match the spatial resolution of the lower-resolution *MS* bands, and $\bar{y}$ is the mean value of the upscaled *PAN*-like band.

Table 2 - Results of the Pearson correlation coefficient between VNIR and SWIR bands.

Bands	Blue	Green	Red	NIR
SWIR1	0.451	0.5	0.519	0.763
SWIR2	0.714	0.749	0.776	0.683

According to the results of *r*, the SWIR1 band exhibits the highest correlation with the NIR band ($r \approx 0.76$), while the SWIR2 band correlates most strongly with the red band ($r \approx 0.78$). Various band fusion algorithms were presented in previous research studies (see Alparone *et al.*, 2008; Vivone *et al.*, 2015; Du *et al.*, 2016; Wang *et al.*, 2016; Kaplan and Avdan, 2018). The high-pass filter (HPF) method (Schowengerdt, 1980) is selected for this study not only due to its widespread application and its ability to extract high-frequency details from higher-resolution data while mitigating low-frequency noise issues (Chavez *et al.*, 1991; Gadal and Gloaguen, 2024) but also because it provides results with accuracy comparable to other filtering techniques (Liu *et al.*, 2022). Therefore, the band fusion is first conducted by means of a downscaling step, in which the SWIR bands are resampled from a 20 m to 10 m spatial resolution using a bilinear interpolation technique, and the NIR and red bands are used as target bands. High-frequency information is incorporated into the lower spatial resolution *MS* through a square box filter (Gangkofner *et al.*, 2008), where the kernel centre value, $c = n \times n - 1$, and the optimal pixel kernel size are based on the ratio of the spatial resolution of *MS* (MS_{sr}) and *PAN*-like bands (PAN_{sr}), $n = 2 \times (MS_{sr}/PAN_{sr}) + 1$. Subsequently, the quality of the band fusion is evaluated using two methods: the *Q*-index, which evaluates the overall quality integrity and similarity of the bands (Wang and Bovik, 2002; Zhao and Liu, 2022), and the Quality with No Reference (*QNR*) index, which quantifies spectral and spatial distortions without the need for reference high-resolution originals (Alparone *et al.*, 2008; Zhao and Liu, 2022). The *Q*-index is calculated, as follows:

$$Q(x,y) = \left(\frac{\sigma_{xy}}{\sigma_x\sigma_y}\right)\left(\frac{2\bar{x}\bar{y}}{\bar{x}^2+\bar{y}^2}\right)\left(\frac{2\sigma_x\sigma_y}{\sigma_x^2+\sigma_y^2}\right) \quad (2)$$

where *Q* ranges from -1 (significant distortion) to 1 (high-quality fusion). The first component corresponds to the correlation coefficient, the second component is the mean luminance between *x* and *y*, and the third component measures the contrast similarity between the bands.

The *QNR*-index is, instead, calculated as follows:

$$QNR = (1 - D_\lambda)^\alpha (1 - D_s)^\beta \quad (3)$$

where *QNR* ranges from 0 (low accuracy) to 1 (high accuracy). Coefficients α and β are two weighted factors, both set to one.

The spectral distortion (D_λ) and the spatial distortion (D_s) vary between 0 (no distortion) and 1 (high distortion):

$$D_\lambda = \sqrt[p]{\frac{1}{N(N-1)} \sum_{i=1}^{N} \sum_{j=1, j \neq i}^{N} \left| Q(MS, other\ MS) - Q\left(MS_f, MS_{downscaled}\right) \right|^p} \quad (4)$$

$$D_s = \sqrt[q]{\frac{1}{N} \sum_{l=1}^{N} \left| Q\left(MS, PAN_{upscaled}\right) - Q\left(MS_f, PAN\right) \right|^q} \quad (5)$$

where *MS* and $PAN_{upscaled}$ are the *MS* and *PAN*-like bands with 20 m spatial resolution, MS_f is the fused *MS* band, $MS_{downscaled}$ and *PAN* are the *MS* and *PAN*-like bands with 10 m resolution. *N* is the number of bands, while *p* and *q* are two positive integer exponents, both set to one.

3.2. Water detection

Various water indices are calculated and compared to determine the most effective one. The band ratio method utilises differences in reflectance (ρ) across distinct wavelengths of light for a given surface. The indices presented in Table 3 are applied using reflectance values from the blue, green, red, NIR, and fused SWIR1 and SWIR2 channels, referred to as ρ_{Blue}, ρ_{Green}, ρ_{Red}, ρ_{NIR}, ρ_{SWIR1}, ρ_{SWIR2}, respectively.

Table 3 - Spectral water indices.

Water indices	Equations	References
Automated water extraction index (AWEI)	$AWEI = \rho_{Blue} + 2.5 \times \rho_{Green} - 1.5 \times (\rho_{NIR} + \rho_{SWIR1}) - 0.25 \times \rho_{SWIR2}$	Feyisa *et al.* (2014)
Desert flood index (DFI) incorporating the normalised difference vegetation index (NDVI)	$DFI = \frac{\rho_{Green} - \rho_{SWIR1} + 0.1}{(\rho_{Green} + \rho_{SWIR1}) \times (NDVI + 0.5)}$ $NDVI = \frac{\rho_{NIR} - \rho_{Red}}{\rho_{NIR} + \rho_{Red}}$	Baig *et al.* (2013) and Rouse *et al.* (1974), respectively
Modified normalised difference water index (MNDWI)	$MNDWI = \frac{\rho_{Green} - \rho_{SWIR1}}{\rho_{Green} + \rho_{SWIR1}}$	Xu (2006)
New water index (NWI)	$NWI = \frac{\rho_{Blue} - (\rho_{NIR} + \rho_{SWIR1} + \rho_{SWIR2})}{\rho_{Blue} + (\rho_{NIR} + \rho_{SWIR1} + \rho_{SWIR2})}$	Ding (2009), as cited in Schwatke *et al.* (2019)
Normalised difference water index (NDWI)	$NDWI = \frac{\rho_{Green} - \rho_{NIR}}{\rho_{Green} + \rho_{NIR}}$	McFeeters (1996)
Water ratio index (WRI)	$WRI = \frac{\rho_{Green} - \rho_{Red}}{\rho_{NIR} + \rho_{SWIR1}}$	Shen and Li (2010)

3.3. Accuracy assessment

The predicted image (i.e. the image derived from spectral indices) is binarised by applying an automated thresholding procedure, conducted at intervals of 0.05 within a range from -1 to 1. This process results in the classification of water pixels with a value of 1, while all other surface types, categorised as non-water, are assigned a value of 0. Next, the building footprint shapefile, retrieved from the Municipality of Santa Fe's database (SF, 2016), is updated using a 2016 Google satellite image and rasterised. In the resulting raster, building footprint pixels are assigned a value of 1, while all other surfaces are assigned a value of 0. Consequently, water pixels that spatially coincide with built-up surfaces are considered misclassified as water and are reclassified as non-water. Thereafter, a majority filter is applied to remove isolated pixels, testing various kernel sizes (3×3, 5×5, and 7×7) in accordance with the recommendations of Dong *et al.* (2006), as well as Hadi and Danoedoro (2021).

Two regions of interest (ROIs), each encompassing 2.69 km^2, are created in water-land interface areas characterised by high vulnerability and recurrent flooding. Within these ROIs, ground data points are randomly generated and the sample size (n_k) is calculated as follows (Krejcie and Morgan, 1970):

$$n_k = \frac{Z^2 N_k p_k (1-p_k)}{(N_k-1)e^2 + Z^2 p_k (1-p_k)} \text{ for } k = 1, 2 \quad (6)$$

where Z is the critical value of the standard normal distribution corresponding to the desired confidence level (95%), specifically 1.96; N_k indicates the total population size of ROI k, equal to 26,900 pixels; p_k denotes the proportion of pixels classified as water within ROI k, assumed to be 0.5; $1 - p_k$ is the proportion of pixels classified as non-water within ROI k; and e^2 is the permitted margin of error, set at 5%. A total of 379 random points are generated for each ROI.

Subsequently, the binary image is compared with three reference images serving as ground truth: natural and false-colour composites, as suggested by Samela *et al.* (2022), and a high-resolution Google Earth image from 14 January 2016 (Fig. 4).

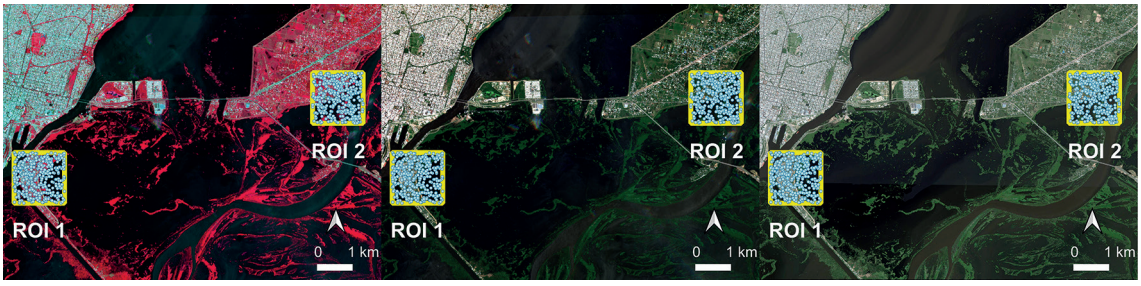

Fig. 4 - A false-colour composite (left), a natural colour composite (centre), and a Google Earth image from 14 January 2016 (right) are taken as reference images and compared with the binary image through random sampling points (cyan points) within two ROIs (yellow squares).

In this comparison, a double-check is conducted to detect typographical errors. Following this, a confusion matrix is created to evaluate the accuracy of the results. The assessment is based on the user accuracy (*UA*), producer accuracy (*PA*), overall accuracy (*OA*), and Kappa coefficient (*k*)

(Cohen, 1960; Congalton, 1991):

$$UA = \frac{TP}{TP + FP} \tag{7}$$

$$PA = \frac{TP}{TP + FN} \tag{8}$$

$$OA = \frac{TP + TN}{n} \tag{9}$$

$$k = \frac{\rho_0 - \rho_e}{1 - \rho_e} \text{ derived from } \rho_0 = \frac{TP + TN}{n} \text{ and } \rho_e = \frac{(TP + FP)(TP + FN) + (FN + TN)(FP + TN)}{n^2} \tag{10}$$

where *TP* corresponds to the pixels correctly classified as water, *FP* the pixels incorrectly classified as water, *FN* the pixels incorrectly classified as non-water, *TN* the pixels correctly classified as non-water, and *n* the total number of sampled pixels.

3.4. Identification of the lowest elevation areas

Upon obtaining the flood map, the analysis focuses on identifying the lowest terrain elevations, which are hypothesised as the primary ingress points of the floodwaters. Subsequently, the binarised image is vectorised to isolate water pixels and delineate the inundation boundary. In accordance with the methodologies presented by Bennani *et al.* (2019) and Samela *et al.* (2022), high-resolution spatial digital elevation models (DEMs) are used to extract ground elevation data. In this study, the vertices delineating the flood extent are extracted and overlaid onto a 2013 DEM with a 5 m spatial resolution and a vertical datum referenced to metre m.s.l., as provided by the Istituto Geografico Nacional. The mean vertical accuracy discrepancy between the DEM and ground control points is –0.51 m. Given the significance of this difference, the DEM is not suitable for precision hydrological studies. Nevertheless, it is effective for identifying terrain variations and detecting the lowest elevation points that are most susceptible to initial water ingress in flood-prone inhabited areas.

4. Results and discussion

4.1. Fused bands

The HPF facilitates the rescaling of the SWIR bands to a spatial resolution of 10 m while preserving spectral information. A comparative analysis is conducted to evaluate the quality of different band fusion configurations using various *PAN*-like bands, specifically the green, red, and NIR bands. The objective is to identify which *PAN*-like band provides the most effective enhancement of the lower-resolution SWIR bands. In this context, the SWIR1 band is fused with the green and NIR bands, whereas the SWIR2 band is fused with the red and NIR bands. These specific fusion combinations, [green-SWIR1], [NIR-SWIR1], and [NIR-SWIR2], are selected to facilitate direct comparison with those previously reported in the literature (Du *et al.*, 2016; Yang *et al.*, 2017), as well as with additional combinations derived from the correlation coefficients presented in Table 2, namely [NIR-SWIR1] and [red-SWIR2]. The resulting fused bands are

subsequently assessed using quality metrics (Table 4) to determine the most spectrally consistent configuration.

Table 4 - Accuracy of the SWIR band fusion based on the *r* results from Eq. (1) and literature references.

Fused bands	**SWIR1**		**SWIR2**	
PAN-like bands	Green	NIR	Red	NIR
Q (MS_{lr}, *other* MS_{lr})	0.500	0.500	0.780	0.780
Q (MS_f, MS_{hr})	0.516	0.474	0.794	0.753
Q (MS_{lr}, PAN_{lr})	0.541	0.766	0.778	0.468
Q (MS_f, PAN_{hr})	0.561	0.792	0.798	0.502
D_λ	0.091	0.112	0.084	0.116
D_S	0.101	0.113	0.100	0.129
QNR	0.816	0.786	0.823	0.769

In terms of correlation (Q), the fusion of SWIR1 with the green band exhibits values ranging from 0.5 to 0.561, whereas fusion with the NIR band achieves values between 0.474 and 0.792. This indicates an improvement in correlation when using the green band due to its lower amplitude. On the other hand, fusion of SWIR2 with the red band shows values ranging between 0.778 and 0.798, whereas with the NIR band, the correlation spans from 0.468 to 0.78, highlighting the superior performance of the red band in the fusion. Metrics D_λ and D_s indicate lower distortions for the fusion of SWIR1 with the green band (0.091 and 0.101) and for the fusion of SWIR2 with the red band (0.084 and 0.1). For the SWIR1 band, the highest fusion accuracy (*QNR* ≈ 0.81) is achieved using the green band, as suggested by Yang *et al.* (2017). In the case of the SWIR2 band, the best accuracy is obtained using the red band (*QNR* ≈ 0.82), as determined by the result of Eq. (1).

4.2. Accuracy of water indices

An assessment of the water indices is conducted to evaluate their effectiveness in detecting water bodies, using various kernel sizes and thresholds. The results are presented using the following metrics: *k*, *OA*, *PA*, and *UA* (Table 5).

The higher values of *k* and *OA* obtained for the *AWEI*, relative to the other indices (see acronyms in Table 3), demonstrate that this index proves to be excellent for detecting water bodies within the study area, especially at the urban-water interface. The minor pixel classification errors observed do not impede the index from obtaining the highest classification accuracy, with a *k* value of 0.949 and an *OA* of 0.974, using a majority filter with a kernel size of 3×3 and a threshold of -0.05. According to the strength ranges proposed by Landis and Koch (1977), the obtained *k* value indicates an almost perfect accuracy of pixel classification. Additionally, this index obtained high values for *PA* at 0.974 and *UA* at 0.971. *MNDWI* also produces consistent results, with a *k* value of 0.893 and an *OA* of 0.947 for a 5×5 kernel size and a threshold of -0.15, demonstrating its efficacy in identifying water pixels. In contrast, *WRI* exhibits the lowest precision, with a *k* value of 0.548 and an *OA* of 0.773, for a kernel size of 7×7 and a threshold of 0.05. Nevertheless, the results of the present study differ from those reported by Fonnegra Mora *et al.* (2021), as they obtained a superior performance for the *WRI* compared to the *MNDWI*. This discrepancy could be explained by differences in image acquisition timing relative to the peak stage of the

Table 5 - Pixel classification accuracy of water indices according to the optimal threshold and kernel sizes.

Water indices	Kernel sizes	Optimal thresholds	*k*	*OA*	*PA*	*UA*
AWEI	3×3	-0.05	0.949	0.974	0.974	0.971
	5×5	-0.1	0.931	0.965	0.988	0.941
	7×7	-0.1	0.912	0.956	0.977	0.932
DFI	3×3	-0.1	0.648	0.828	0.653	0.970
	5×5	-0.1	0.662	0.835	0.664	0.975
	7×7	-0.1	0.662	0.835	0.664	0.975
MNDWI	3×3	-0.15	0.885	0.943	0.912	0.964
	5×5	-0.15	0.893	0.947	0.918	0.967
	7×7	-0.15	0.888	0.944	0.918	0.961
NWI	3×3	-0.7	0.826	0.914	0.859	0.953
	5×5	-0.7	0.832	0.916	0.859	0.959
	7×7	-0.7	0.826	0.914	0.850	0.961
NDWI	3×3	-0.25	0.813	0.907	0.853	0.943
	5×5	-0.25	0.824	0.912	0.859	0.950
	7×7	-0.2	0.815	0.908	0.828	0.973
WRI	3×3	0.05	0.525	0.761	0.825	0.711
	5×5	0.05	0.532	0.765	0.828	0.715
	7×7	0.05	0.548	0.773	0.833	0.723

event or by the absence of band fusion in their methodology. In contrast, the findings of the present study indicate that *AWEI* and *MNDWI* exhibit the highest robustness in detecting water under the analysed conditions. Consequently, the results derived from *AWEI* are utilised in the following phases of the study (Fig. 5).

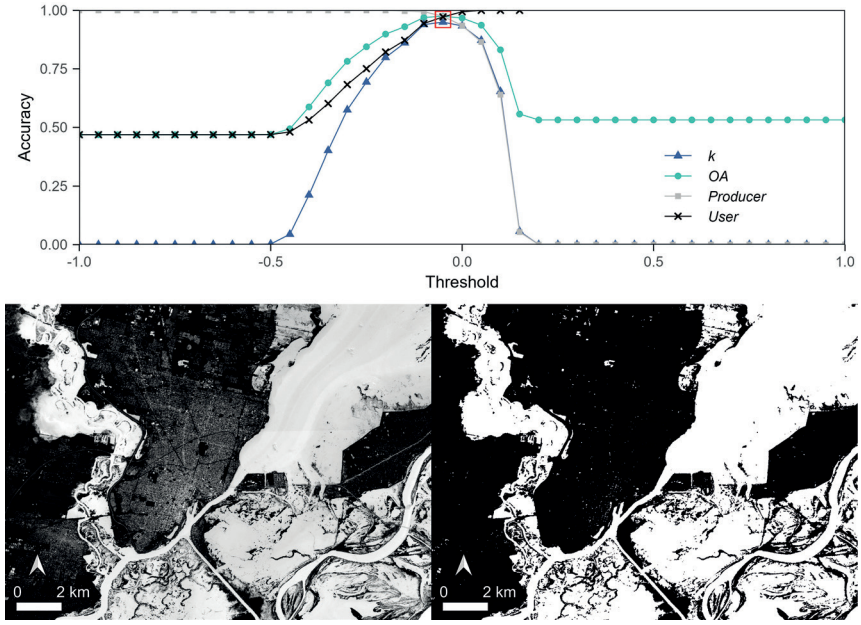

Fig. 5 - *AWEI* results with the optimal threshold identified in the red rectangle (top), the predicted image (left), and the binarised image (right) showing water pixels in white and non-water pixels in black.

4.3. Flood access points

The results indicate that on 13 January 2016, the floodwaters covered an estimated spatial extent of approximately 170 km^2 in the study area, which has a total surface area of 360 km^2. This flood event affected various areas within the La Costa district (as delineated by the dashed outline in Fig. 6) and the north-western shoreline of the Setúbal Lagoon.

The accurate delineation of the floodline enables the identification of the most vulnerable areas (red polygons in Fig. 6). The findings suggest that water infiltrated through the lowest terrain elevations in Playa Norte (14.3 m m.s.l.), Colastiné Norte (14.1 m m.s.l.), Colastiné Sur (13.5 m m.s.l. and 14 m m.s.l.), Bajada di Stefano (13.8 m m.s.l., 14.4 m m.s.l., and 15.1 m m.s.l.),

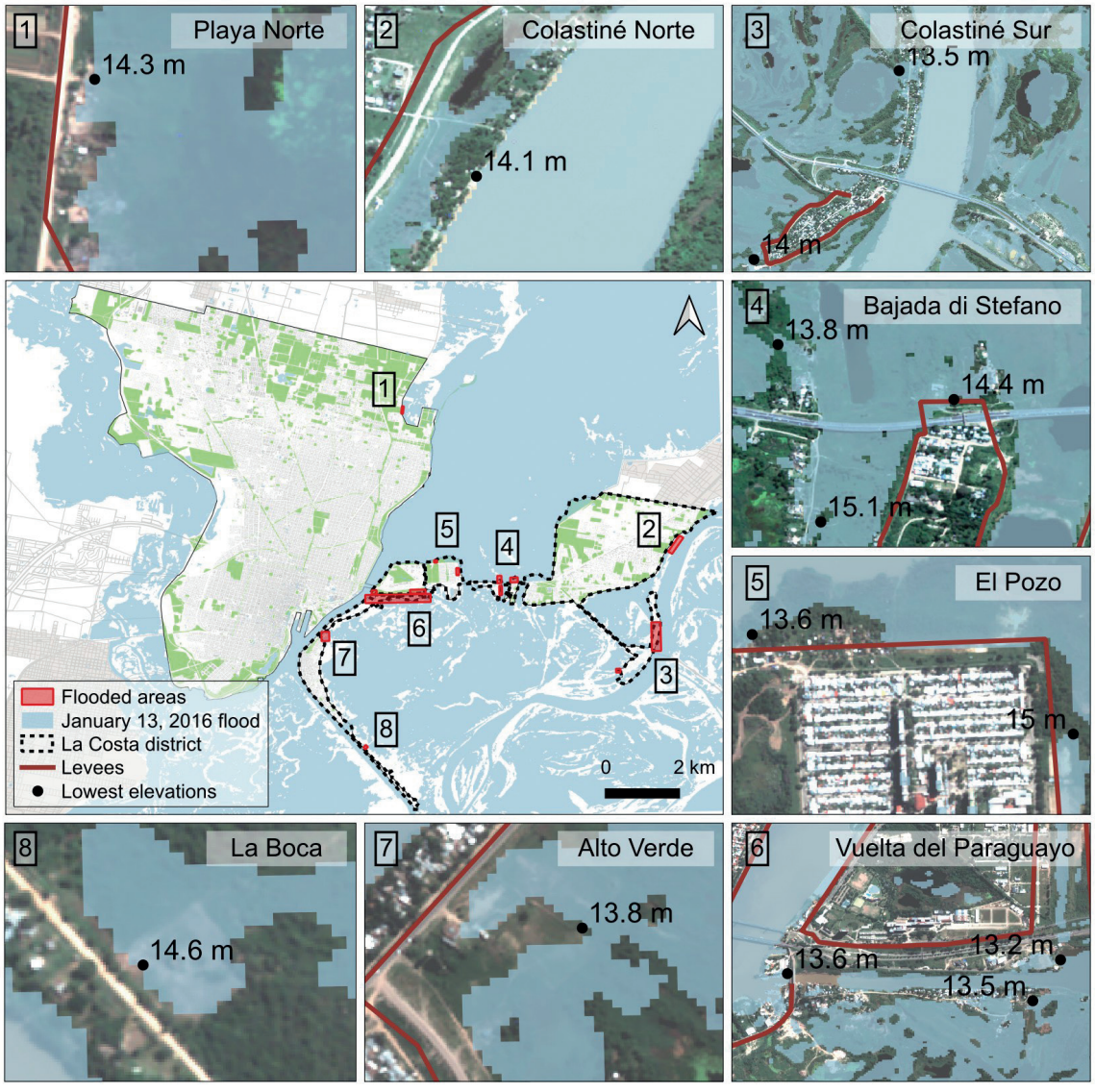

Fig. 6 - Spatial extent of the 13 January 2016 flood (light blue polygon), with the minimum ground elevations (black points, in metre m.s.l.) reached by the floodline within the flooded areas (red polygons) adjacent the levee perimeter (brown lines). The background features a 2024 satellite image from Pléiades, showing currently inhabited areas.

El Pozo (13.6 m m.s.l. and 15 m m.s.l.), Vuelta del Paraguayo (13.2 m m.s.l., 13.5 m m.s.l., and 13.6 m m.s.l.), Alto Verde (13.8 m m.s.l.), and La Boca (14.6 m m.s.l.).

Considering that these areas are all located outside the flood defence levee enclosures (brown lines in Fig. 6), low topography appears to be the principal factor in increasing vulnerability. Moreover, the levees were not overtopped, as evidenced by a comparison between the crest elevations reported by the Ministry of Federal Planning, Public Investment and Services (2009) and the maximum flood levels recorded by the gauges on 8 January 2016 (Table 1). There is a discrepancy of 2.46 m between the elevation of the nearest levee crest and the peak level recorded by the gauge at Setúbal Lagoon, and a discrepancy of 0.49 m between the elevation of the nearest levee crest and the gauge record at the Colastiné River. Furthermore, according to internal reports from the Department of Risk Management of the Municipality of Santa Fe, the evacuation protocol of the flood-affected areas was activated in Colastiné Sur on 26 December 2015, followed by Playa Norte and La Boca on 2 January 2016, and finally Bajada di Stefano on 4 January. A total of 746 inhabitants were evacuated (Ministry of Health, 2016). The flood levels remained above the alert threshold until 9 March 2016, followed by a gradual decrease. Nevertheless, between 20 March and 13 May, a resurgence in water levels was observed; however, neither the Setúbal Lagoon nor the Colastiné River reached the peak levels recorded in January 2016.

These identified flood-prone areas are the first to experience inundation during river floods, primarily due to the spatial positioning of settlements located outside the levee system and their unfavourable topographical conditions. Nevertheless, the land subdivision of these flood-prone areas is increasing, which is alarming given the potential for severe floods that may exceed the 2016 event. Therefore, it is imperative to study historical floods, considering them as reference cases to inform and enhance prevention strategies for future severe flooding, given that Santa Fe has experienced flood events in the 20th century and earlier that surpassed both the discharge and water levels recorded during the 2016 event (Bello *et al.*, 2018; Snaider and Ramírez, 2018). Under such circumstances, the implementation of flood warning signage is recommended to indicate the locations of the lowest-lying areas, informing the population of the necessity to evacuate upon activation of the established protocol. Additionally, expanding upon the findings of Mendizabal (2018), permanent evacuation routes should be strategically designed from these identified points to optimise coordination in emergency response planning, ensuring effective evacuation in the event of an extreme flood event.

The incorporation of spatial analysis into flood risk management offers a more comprehensive understanding of the Paraná River flooding events impacting the city of Santa Fe. Enhancing the understanding of past flood events enables the predictive assessment of future extreme floods and informs evidence-based decision-making strategies to strengthen the resilience of Santa Fe.

5. Concluding remarks

The city of Santa Fe experienced a Paraná River flood in January 2016 during the EN15-16, affecting several low-lying areas. Despite this, the city lacks an accurate record of the spatial extent of this flood. This study addresses this gap by estimating the inundated areas using Sentinel-2 imagery acquired shortly after the flood peak observed in the Setúbal Lagoon and Colastiné River. Additionally, a band fusion is performed to enhance the spatial resolution of the SWIR1 and SWIR2 bands. The HPF method improves the spatial resolution of these

two bands without introducing significant spectral distortion, achieving an accuracy exceeding 81% (*QNR* > 0.81, see Table 4) and enhancing flood delineation. Additionally, various spectral indices are compared to determine the one yielding the highest classification accuracy for pixels. *AWEI* effectively classifies water pixels, achieving an overall accuracy of 97.4% and a Kappa coefficient of 94.9%, indicating an almost perfect estimation of the flood extent. These methodologies are recommended for evaluating areas with characteristics analogous to those of Santa Fe.

The findings reveal that the most impacted areas correspond to the La Costa district and the northern coast of the city of Santa Fe lapped by the Setúbal Lagoon, both located outside the levee system. Considering the recent wet phase associated with the ENSO, these areas remain significantly vulnerable to future flood events. Furthermore, climate change is projected to intensify the severity and recurrence of flood events, exacerbating associated devastating consequences due to the rapid demographic growth and urban sprawl in flood-prone areas. This is particularly concerning given that, during the most recent LN event (2019-2023), land parcels adjacent to the minor bed of the Colastiné River were sold, thereby increasing population density in very high-risk areas.

This study highlights the significant role of remote sensing in near-real-time flood monitoring and urban flood risk assessment. These methodologies are essential for enhancing existing evacuation strategies and implementing educational measures to reinforce public awareness for future floods. Additionally, this approach is applicable to all riverfront cities, providing valuable insights for urban flood risk management in similar environments. This research is expected to enhance our understanding of Paraná River floods, as adequate preparedness could mitigate the impacts of future events potentially exceeding extreme conditions recorded in the past.

Acknowledgments. The author would like to thank the Airbus DS Geo (https://intelligence.airbus.com/) for providing access to the Pléiades satellite imagery.

REFERENCES

Abou Rafee S.A., Uvo C.B., Martins J.A., Machado C.B. and Freitas E.D.; 2022: *Land use and cover changes versus climate shift: who is the main player in river discharge? A case study in the upper Paraná River Basin*. J. Environ. Manage., 309, 114651, doi: 10.1016/j.jenvman.2022.114651.

Aire Digital; 2020: *Loteo irregular: denuncian que vendieron terrenos inundables en Colastiné Sur*. Aire Digital, Santa Fe, https://www.airedesantafe.com.ar/santa-fe/loteo-irregular-denuncian-que-vendieron-terrenos-inundables-colastine-sur-n177240.

Alganci U., Sertel E. and Kaya S.; 2019: *Determination of the flooded agricultural lands with spot 6 high resolution satellite images: a case study of Menderes Plain, Turkey*. In: Proc. 8th International Conference on Agro-Geoinformatics, Agro-Geoinformatics 2019, Institute of Electrical and Electronics Engineers Inc., Istanbul, Turkey, doi: 10.1109/Agro-Geoinformatics.2019.8820242.

Alparone L., Aiazzi B., Baronti S., Garzelli A., Nencini F. and Selva M.; 2008: *Multispectral and panchromatic data fusion assessment without reference*. Photogramm. Eng. Remote Sens., 74, 193-200, doi: 10.14358/PERS.74.2.193.

Amarasekera K.N., Lee R.F., Williams E.R. and Eltahir E.A.B.; 1997: *ENSO and the natural variability in the flow of tropical rivers*. J. Hydrol., 200, 24-39, doi: 10.1016/S0022-1694(96)03340-9.

Anderson R.J. Jr, da Franca Ribeiro dos Santos N. and Diaz H.F.; 1993: *An analysis of flooding in the Paraná/Paraguay River basin*. LATEN Dissemination Note 5, Latin Am. and Caribbean Tech. Dep., Environ. Div., World Bank, Washington, DC, USA, 68 pp.

Arias P.A., Bellouin N., Coppola E., Jones R.G., Krinner G., Marotzke J., Naik V., Palmer M.D., Plattner G.-K., Rogelj J., Rojas M., Sillmann J., Storelvmo T., Thorne P.W., Trewin B., Achuta Rao K., Adhikary B., Allan R.P., Armour K., Bala G., Barimalala R., Berger S., Canadell J.G., Cassou C., Cherchi A., Collins W., Collins W.D., Connors S.L., Corti S., Cruz F., Dentener F.J., Dereczynski C., Di Luca A., Diongue Niang A., Doblas-Reyes F.J., Dosio A., Douville H., Engelbrecht F., Eyring V., Fischer E., Forster P., Fox-Kemper B., Fuglestvedt J.S., Fyfe J.C., Gillett N.P., Goldfarb L., Gorodetskaya I., Gutierrez J.M., Hamdi R., Hawkins E., Hewitt H.T., Hope P., Islam A.S., Jones C., Kaufman D.S., Kopp R.E., Kosaka Y., Kossin J., Krakovska S., Lee J-Y., Li J., Mauritsen T., Maycock T.K., Meinshausen M., Min S.-K., Monteiro P.M.S., Ngo-Duc T., Otto F., Pinto I., Pirani A., Raghavan K., Ranasinghe R., Ruane A.C., Ruiz L., Sallée J.-B., Samset B.H., Sathyendranath S., Seneviratne S.I., Sörensson A.A., Szopa S., Takayabu I., Tréguier A.-M., van den Hurk B., Vautard R., von Schuckmann K., Zaehle S., Zhang X. and Zickfeld K.; 2021: *Technical Summary.* In: Masson-Delmotte V., Zhai P., Pirani A., Connors S.L., Péan C., Berger S., Caud N., Chen Y., Goldfarb L., Gomis M.I., Huang M., Leitzell K., Lonnoy E., Matthews J.B.R., Maycock T.K., Waterfield T., Yelekçi O., Yu R. and Zhou B. (eds.), Climate change 2021: the physical science basis. Contribution of working group to the sixth assessment report of the intergovernmental panel on climate change. Cambridge University Press, Cambridge, UK and New York, NY, USA, pp. 33-144, doi: 10.1017/9781009157896.002.

Auwalu F.K., Wu Y., Ghali A.A., Roknisadeh H. and Akram A.N.A.; 2021: *Analyzing urban growth and land cover change scenario in Lagos, Nigeria using multi-temporal remote sensing data and GIS to mitigate flooding*. Geomatics, Nat. Hazards and Risk, 12, 631-652, doi: 10.1080/19475705.2021.1887940.

Baez Ullberg S.; 2017: *Forgetting flooding? Post-disaster livelihood and embedded. Remembrance in suburban Santa Fe, Argentina*. Nat. Clim., 12, 27-45, doi: 10.3167/nc.2017.120103.

Baig M.H.A., Zhang L., Wang S., Jiang G., Lu S. and Tong Q.; 2013: *Comparison of MNDWI and DFI for water mapping in flooding season*. In: Proc. IEEE International Geoscience and Remote Sensing Symposium, Melbourne, Australia, pp. 2876-2879, doi: 10.1109/IGARSS.2013.6723425.

Bello O.D., Ballesteros J., Buitrago M., González M. and Velasco O.; 2018: *Análisis retrospectivo de las inundaciones: lecciones y recomendaciones*. Comisión Económica Para América Latina y el Caribe (CEPAL), Ministerio del Interior, Obras Públicas y Vivienda, Banco Interamericano de Desarrollo (BID). Documentos de Proyectos, 54 pp.

Bennani O., Tramblay Y., Saidi M. and Leone F.; 2019: *Flood hazard mapping using two digital elevation models: application in a semi-arid environment of Morocco*. Eur. Sci. J., 15, 338-359, doi: 10.19044/esj.2019.v15n33p338.

Boulanger J.-P., Leloup J., Penalba O., Rusticucci M., Lafon F. and Vargas W.; 2005: *Observed precipitation in the Paraná-Plata hydrological basin: long-term trends, extreme conditions and ENSO teleconnections*. Clim. Dyn., 24, 393-413, doi: 10.1007/s00382-004-0514-x.

CDSE (Copernicus Data Space Ecosystem); n.d.: *Copernicus Data Space Ecosystem.* https://dataspace.copernicus.eu.

Camilloni I.A. and Barros V.R.; 2003: *Extreme discharge events in the Paraná River and their climate forcing*. J. Hydrol., 278, 94-106, doi: 10.1016/S0022-1694(03)00133-1.

Chavez P. Jr, Sides S.C. and Anderson J.A.; 1991: *Comparison of three different methods to merge multiresolution and multispectral data: Landsat TM and SPOT panchromatic*. Photogramm. Eng. Remote Sens., 57, 265-303.

Cohen J.; 1960: *A coefficient of agreement for nominal scales*. Educ. Psycholog. Meas., 20, 37-46.

Congalton R.G.; 1991: *A review of assessing the accuracy of classifications of remotely sensed data*. Remote Sens. Environ., 37, 35-46, doi: 10.1016/0034-4257(91)90048-B.

Crovella F. and Acebal A.; 2018: *Inundaciones recurrentes, territorialidades emergentes y desalojos latentes. Conflictos del habitar en el barrio La Vuelta del Paraguayo, de la ciudad de Santa Fe, a principios del siglo XXI*. Cuaderno urbano, 25, 51-72, doi: 10.30972/crn.25253511.

D'Arrigo R., Cook E.R., Wilson R.J., Allan R. and Mann M.E.; 2005: *On the variability of ENSO over the past six centuries*. Geophys. Res. Lett., 32, L03711, doi: 10.1029/2004GL022055.

De Majo V.; 2022: *Institutional conditions for building proactive flood management: lessons from Santa Fe in Argentina*. Int. J. Disaster Risk Reduction, 81, 103251, doi: 10.1016/j.ijdrr.2022.103251.

Depetris P.J.; 2007: *The Parana River under extreme flooding: a hydrological and hydro-geochemical insight*. Interciencia, 32, 656-662.

Depetris P.J., Kempe S., Latif M. and Mook W.G.; 1996: *ENSO-controlled flooding in the Paraná River (1904-1991)*. Naturwissenschaften, 83, 127-129, doi: 10.1007/BF01142177.

Dong R., Dong J., Wu G. and Deng H.; 2006: *Optimization of post-classification processing of high-resolution satellite image: a case study*. Sci. China: Series E Technol. Sci., 49, 98-107, doi: 10.1007/s11431-006-8111-3.

Du Y., Zhang Y., Ling F., Wang Q., Li W. and Li X.; 2016: *Water bodies' mapping from Sentinel-2 imagery with modified normalized difference water index at 10-m spatial resolution produced by sharpening the SWIR band*. Remote Sens., 8, 354, doi: 10.3390/rs8040354.

Erkoç M.H.; 2023: *A scientific analysis on the water levels of Lake Beyşehir and drought conditions in the area*. Bull. Geoph. Ocean., 66, 317-330, doi: 10.4430/bgo00426.

Ferral A., Luccini E., Aleksinkó A. and Scavuzzo C.M.; 2019: *Flooded-area satellite monitoring within a Ramsar wetland nature reserve in Argentina*. Remote Sens. Appl.: Soc. Environ., 15, 100230,, doi: 10.1016/j.rsase.2019.04.003.

Feyisa G.L., Meilby H., Fensholt R. and Proud S.R.; 2014: *Automated water extraction index: a new technique for surface water mapping using landsat imagery*. Remote Sens. Environ., 140, 23-35, doi: 10.1016/j.rse.2013.08.029.

Filippi M.E.; 2022: *A role for municipal governments in leveraging transformative change for urban disaster risk management: the experience of Santa Fe, Argentina, with urban flood risk*. Clim. Risk Manage., 35, 100397, doi: 10.1016/j.crm.2022.100397.

Fonnegra Mora D.C., Walker E. and Venturini V.; 2021: *Flood monitoring in Santa Fe using the Google Earth Engine platform*. In: Proc. XIX Workshop on Information Processing and Control (RPIC), San Juan, Argentina, pp. 1-6, doi: 10.1109/RPIC53795.2021.9648518.

Gadal S. and Gloaguen T.; 2024: *Performance of Landsat 8 OLI and Sentinel 2 MSI images based on MNF versus PCA algorithms and convolution operators for automatic Lithuanian coastline extraction*. SN Comput. Sci., 5, 308, doi: 10.1007/s42979-024-02623-9.

Gangkofner U.G., Pradhan P.S. and Holcomb D.W.; 2008: *Optimizing the high-pass filter addition technique for image fusion*. Photogramm. Eng. Remote Sens., 74, 1107-1118, doi: 10.14358/PERS.74.9.1107.

Gardiol M. and del Valle Morresi M.; 2023: *Structural and non-structural measures implemented in the Santa Fe coastal embankment. Period 1900-2020*. Revista de Estudios Latinoamericanos sobre Reducción del Riesgo de Desastres REDER, 7, 61-76, doi: 10.55467/reder.v7i1.108.

Gergis J., Braganza K., Fowler A., Mooney S. and Risbey J.; 2006: *Reconstructing El Niño-Southern Oscillation (ENSO) from high-resolution palaeoarchives*. J. Quat. Sci., 21, 707-722, doi: 10.1002/jqs.1070.

Graosque J.Z. and Guasselli L.A.; 2020: *Principal component analysis of C-SAR images for flood mapping - Santa Fe province, Argentina*. Territorium, 27, 41-48, doi: 10.14195/1647-7723_27-2_4.

Hadi H.A. and Danoedoro P.; 2021: *Comparing several pixel-based classification methods for vegetation structural composition mapping using Sentinel 2A imagery in Salatiga area, central Java*. In: Proc. SPIE 12082, 7th Geoinformation Science Symposium 2021, Yogyakarta, Indonesia, 120820T, doi: 10.1117/12.2621965.

Hijmans R.; 2023: *Raster: geographic data analysis and modeling*. R package version 3.6-32, https://CRAN.R-project.org/web/packages/raster/index.html, doi: 10.32614/CRAN.package.raster.

Honorable Municipal Council of the City of Santa Fe de la Vera Cruz; 2018: *Ordinance n°. 12591: Reglamento de ordenamiento urbano de la Ciudad de Santa Fe de la Vera Cruz*, 6 pp., https://www.concejosantafe.gov.ar/wp-content/uploads/Ordenanza/Ordenanza_12591.pdf.

Hurtado S.I., Agosta E.A. and Zaninelli P.G.; 2023: *Monthly variations of forcing mechanisms of austral summer precipitation in subtropical Argentina.* Atmos. Res., 285, 106609, doi: 10.1016/j.atmosres.2023.106609.

INDEC (Instituto Nacional de Estadística y Censos de la República Argentina); 2023: *Censo nacional de población, hogares y viviendas 2022. Resultados definitivos. Indicadores demográficos, por sexo y edad, 1st ed.* Buenos Aires, Argentina, 98 pp., https://www.indec.gob.ar.

Isla F.I.; 2018: *ENSO-triggered floods in south America: correlation between maximum monthly discharges during strong events*. Hydrol. Earth Syst. Sci., 13 pp., doi: 10.5194/hess-2018-107.

Jain S.K., Singh R.D., Jain M.K. and Lohani A.K.; 2005: *Delineation of flood-prone areas using remote sensing techniques*. Water Resour. Manage., 19, 333-347, doi: 10.1007/s11269-005-3281-5.

Ji L., Zhang L. and Wylie B.; 2009: *Analysis of dynamic thresholds for the normalized difference water index*. Photogramm. Eng. Remote Sens., 75, 1307-1317, doi: 10.14358/PERS.75.11.1307.

Kabeja C., Li R., Rwatangabo D.E.R. and Duan J.; 2022: *Monitoring land use/cover changes by using multi-temporal remote sensing for urban hydrological assessment: a case study in Beijing, China*. Remote Sens., 14, 4273, doi: 10.3390/rs14174273.

Kaplan G. and Avdan U.; 2018: *Sentinel-2 pan sharpening - Comparative analysis*. Proc., 2, 345, doi: 10.3390/ecrs-2-05158.

Khalid H.W., Zahid Khalil R.M. and Qureshi M.A.; 2021: *Evaluating spectral indices for water bodies extraction in western Tibetan Plateau*. Egypt. J. Remote Sens. Space Sci., 24, 619-634, doi: 10.1016/j.ejrs.2021.09.003.

Krejcie R.V. and Morgan D.W.; 1970: *Determining sample size for research activities*. Educ. Psycholog. Meas., 30, 607-610, doi: 10.1177/0013164470030003.

Landis J.R. and Koch G.G.; 1977: *The measurement of observer agreement for categorical data*. Biometrics, 33, 159-174.

Liu H., Hu H., Liu X., Jiang H., Liu W. and Yin X.; 2022: *A comparison of different water indices and band downscaling methods for water bodies mapping from Sentinel-2 imagery at 10-m resolution*. Water, 14, 2696, doi: 10.3390/w14172696.

Lovino M.A., Müller G.V., Pierrestegui M.J., Espinosa E. and Rodríguez L.; 2022: *Extreme precipitation events in the Austral Chaco region of Argentina*. Int. J. Clim., 42, 5985-6006, doi: 10.1002/joc.7572.

Martínez R., Zambrano E., Nieto J.J., Hernández J. and Costa F.; 2017: *Evolution, vulnerability and the economic and social impacts of El Niño 2015-2016 in Latin America*. Invest. Geográficas, 68, 65-78, doi: 10.14198/INGEO2017.68.04.

Mason D.C., Dance S.L. and Cloke H.L.; 2021: *Floodwater detection in urban areas using Sentinel-1 and WorldDEM data*. J. Appl. Remote Sens., 15, 032003, doi: 10.1117/1.JRS.15.032003.

McFeeters S.K.; 1996: *The use of the normalized difference water index (NDWI) in the delineation of open water features*. Int. J. Remote Sens., 17, 1425-1432, doi: 10.1080/01431169608948714.

Mendizabal S.; 2018: *Propuesta de estrategia de evacuación para la ciudad de Santa Fe frente a una crecida extraordinaria: un análisis con SIG*. El Ojo del Cóndor, IGN, 9, 25-27.

Ministry of Federal Planning, Public Investment and Services; 2009: *Evaluación del estado y grado de protección del Sistema de Defensa de las ciudades de Santa Fe - Recreo y anillos de la Ruta Prov. n° 1*. Final report.

Ministry of Health; 2016: *Informe de situación de la contingencia hídrica, provincia de Santa Fe*. Report n° 3, 7 pp.

Montanher O.C., Minaki C., de Morais E.S., de Paula Silva J. and Pereira P.; 2023: *Geosystemic impacts of the extreme rainfall linked to the El Niño 2015/2016 event in northern Paraná, Brazil*. Appl. Sci., 13, 9678, doi: 10.3390/app13179678.

Neffen G.; 2016: *Cuáles son los puntos vulnerables de la ciudad frente a una crecida*. El Litoral, https://www.ellitoral.com/index.php/diarios/2016/02/16/metropolitanas/AREA-01.html.

Pántano V.C., Holzman M.E., Penalba O.C. and Rivas R.; 2022: *ENSO signal on subseasonal precipitation distribution and soil moisture response in the Argentine Pampas*. Pure Appl. Geophys., 179, 879-896, doi: 10.1007/s00024-022-02949-6.

Pasquini A.I. and Depetris P.J.; 2010: *ENSO-triggered exceptional flooding in the Paraná River: where is the excess water coming from?* J. Hydrol., 383, 186-193, doi: 10.1016/j.jhydrol.2009.12.035.

Pebesma E.; 2018: *Simple features for R: standardized support for spatial vector data*. R J., 10, 439-446, doi: 10.32614/RJ-2018-009.

Prieto M.; 2007: *ENSO signals in south America: rains and floods in the Paraná River region during colonial times*. Clim. Change, 83, 39-54, doi: 10.1007/s10584-006-9188-1.

Rouse J.W. Jr, Haas R.H., Schell J.A. and Deering D.W.; 1974: *Monitoring vegetation systems in the Great Plains with ERTS*. In: Proc. NASA. Goddard Space Flight Center 3d ERTS-1 Symp., Vol. 1, Sect. A, PAPER-A20, pp. 309-317.

Samela C., Coluzzi R., Imbrenda V., Manfreda S. and Lanfredi M.; 2022: *Satellite flood detection integrating hydrogeomorphic and spectral indices*. GISci. Remote Sens., 59, 1997-2018, doi: 10.1080/15481603.2022.2143670.

Santoso A., McPhaden M.J. and Cai W.; 2017: *The defining characteristics of ENSO extremes and the strong 2015/2016 El Niño*. Rev. Geophys., 55, 1079-1129, doi: 10.1002/2017RG000560.

Schowengerdt R.A.; 1980: *Reconstruction of multispatial, multispectral image data using spatial frequency content*. Photogramm. Eng. Remote Sens., 46, 1325-1334.

Schwatke C., Scherer D. and Dettmering D.; 2019: *Automated extraction of consistent time-variable water surfaces of lakes and reservoirs based on Landsat and Sentinel-2*. Remote Sens., 11, 1010, doi: 10.3390/rs11091010.

SF (Municipalidad de Santa Fe); 2016: *El Comité de Emergencia Hídrica dio detalles sobre la situación en la provincia.* Gestion Santa Fe Provincia, https://www.santafe.gov.ar/noticias/noticia/223715.

Shen L. and Li C.; 2010: *Water body extraction from Landsat ETM+ imagery using Adaboost algorithm*. In: Proc. IEEE 18th International Conference on Geoinformatics: GIScience in Change, Geoinformatics, Peking University, Beijing, China, pp. 1-4, doi: 10.1109/GEOINFORMATICS.2010.5567762.

Snaider P.P. and Ramírez M.L.; 2018: *Altura de las aguas en épocas de creciente y estiaje*. El Ojo del Cóndor, IGN, 9, 16-19.

SNIH (Sistema Nacional de Información Hídrica); 2025: *Datos históricos de la red hidrológica nacional, Argentina.* https://snih.hidricosargentina.gob.ar.

Subraelu P., Ahmed A., Ebraheem A.A., Sherif M., Mirza S.B., Ridouane F.L. and Sefelnasr A.; 2023: *Risk assessment and mapping of flash flood vulnerable zones in arid region, Fujairah City, UAE-using remote sensing and GIS-based analysis*. Water, 15, 2802, doi: 10.3390/w15152802.

Sukojo B.M. and Alfiansyah F.; 2017: *Flood disaster analysis using Landsat-8 and SPOT-6 imagery for determination of flooded areas in Sampang, Madura*. IOP Conf. Ser.: Earth Environ. Sci., 98, 012021, doi: 10.1088/1755-1315/98/1/012021.

Tanim A.H., McRae C.B., Tavakol-Davani H. and Goharian E.; 2022: *Flood detection in urban areas using satellite imagery and machine learning*. Water, 14, 1140, doi: 10.3390/w14071140.

Tucci C.E.M. and Clarke R.T.; 1998: *Environmental issues in the la Plata Basin*. Int. J. Water Resour. Dev., 14, 157-173.

UNDRR; 2015: *Sendai framework for disaster risk reduction 2015-2030*. United Nations Office for Disaster Risk Reduction, Geneva, Switzerland, 32 pp., https://www.undrr.org/publication/sendai framework-disaster-risk-reduction-2015-2030.

Vivone G., Alparone L., Chanussot J., Dalla Mura M., Garzelli A., Licciardi G.A., Restaino R. and Wald L.; 2015: *A critical comparison among pansharpening algorithms*. IEEE Trans. Geosci. Remote Sens., 53, 2565-2586, doi: 10.1109/TGRS.2014.2361734.

Wang Q., Shi W., Li Z. and Atkinson P.M.; 2016: *Fusion of Sentinel-2 images*. Remote Sens. Environ., 187, 241-252, doi: 10.1016/j.rse.2016.10.030.

Wang Z. and Bovik A.C.; 2002: *A Universal image quality index*. IEEE Signal Process. Lett., 9, 81-84, doi: 10.1109/97.995823.

Wickham H.; 2016: *ggplot2: elegant graphics for data analysis*. Springer-Verlag New York, NY, USA, 276 pp., doi: 10.1007/978-3-319-24277-4_9.

Wickham H. and Henry L.; 2023: *purrr: functional programming tools*. R package version 1.2.1, https://CRAN.R-project.org/web/packages/purrr/index.html., doi: 10.32614/CRAN.package.purrr.

Wickham H., François R., Henry L., Müller K. and Vaughan D.; 2023: *dplyr: a grammar of data manipulation*. R package version 1.2.0, https://CRAN.R-project.org/web/packages/dplyr/index.html., doi: 10.32614/CRAN.package.dplyr.

Xu H.; 2006: *Modification of normalised difference water index (NDWI) to enhance open water features in remotely sensed imagery*. Int. J. Remote Sens., 27, 3025-3033, doi: 10.1080/01431160600589179.

Yang X., Zhao S., Qin X., Zhao N. and Liang L.; 2017: *Mapping of urban surface water bodies from Sentinel-2 MSI imagery at 10 m resolution via NDWI-based image sharpening*. Remote Sens., 9, 596, doi: 10.3390/rs9060596.

Zhang H., Qi Z., Li X., Chen Y., Wang X. and He Y.; 2021: *An urban flooding index for unsupervised inundated urban area detection using Sentinel-1 Polarimetric SAR images*. Remote Sens., 13, 4511, doi: 10.3390/rs13224511.

Zhao J., Li Y., Matgen P., Pelich R., Hostache R., Wagner W. and Chini M.; 2022: *Urban-aware U-Net for large-scale urban flood mapping using multitemporal Sentinel-1 intensity and interferometric coherence*. IEEE Trans. Geosci. Remote Sens., 60, 1-21, doi: 10.1109/TGRS.2022.3199036.

Zhao Y. and Liu D.; 2022: *A robust and adaptive spatial-spectral fusion model for PlanetScope and Sentinel-2 imagery*. Gisci. Remote Sens., 59, 520-546, doi: 10.1080/15481603.2022.2036054.

Corresponding author: Sophie Mendizabal
Department of Risk Management, Municipality of Santa Fe
Salta 2951, S3000 Santa Fe de la Vera Cruz, Argentina
Phone: +59 4 155024446; e-mail: s.mendizabal@santafeciudad.gov.ar